Estimating regional scale methane flux and budgets using CARVE aircraft measurements over Alaska

Sean Hartery[1], Róisín Commane[2], Jakob Lindaas[2], Colm Sweeney[3,4], John Henderson[5], Marikate Mountain[5], Nicholas Steiner[6], Kyle McDonald[6], Steven J. Dinardo[7], Charles E. Miller[7], Steven C. Wofsy[2], and Rachel Y.-W. Chang[1,2]

[1]Department of Physics and Atmospheric Science, Dalhousie University, Halifax NS
[2]School of Engineering and Applied Sciences, Harvard University, Cambridge MA
[3]Global Monitoring Division, National Oceanic and Atmospheric Administration Earth System Research Laboratory, Boulder CO
[4]Cooperative Institute for Research in Environmental Sciences, University of Colorado, Boulder CO
[5]Atmospheric and Environmental Research, Inc., Lexington, MA
[6]Department of Earth and Atmospheric Science, City College University of New York, New York NY
[7]Jet Propulsion Laboratory, California Institute of Technology, Pasadena CA

Correspondence to: R.Y.-W. Chang (rachel.chang@dal.ca)

Abstract. Methane (CH_4) is the second most important greenhouse gas but their emissions from northern regions is still poorly constrained. In this study, we analyze a subset of in situ CH_4 aircraft observations made over Alaska during the growing seasons of 2012–2014 as part of the Carbon in Arctic Reservoir Vulnerability Experiment (CARVE). Surface CH_4 fluxes are estimated using an atmospheric particle transport model which quantitatively links surface emissions from Alaska and the western Yukon

5 with observations of enhanced CH_4 in the boundary layer. We estimate that between May and September, 2.1±0.5 Tg, 1.7±0.4 Tg and 2.0 ±0.3 Tg of CH_4 were emitted from the region of interest for 2012–2014, respectively. The predominant sources of the CH_4 budget were two broadly classed eco-regions within our domain, with CH_4 from the tundra region accounting for over half of the overall budget, despite only representing 18% of the total surface area. Boreal regions, which cover a large part of the study region, accounted for the remainder of the emissions. Simple multiple linear regression analysis revealed that

10 overall, CH_4 flux were largely driven by soil temperature and elevation. In regions specifically dominated by wetlands, soil temperature and moisture at 10 cm depth were important explanatory variables while in regions that were not wetlands, soil temperature and moisture at 40 cm depth were more important, reflecting the depth at which methanogenesis occurs. Although similar variables have been found in the past to control CH_4 emissions at local scales, this study shows that they can be used to generate a statistical model to estimate the regional scale CH_4 budget.

15 # 1 Introduction

Recent trends in observed global atmospheric methane (CH_4) mole fractions have shown increases since a short-lived stabilization period in the early 2000's and have increased by ∼150% from pre-industrial values (Dlugokencky et al., 2011; Kirschke et al., 2013; Ciais et al., 2014). As the second most potent anthropogenically-emitted greenhouse gas after carbon dioxide

Atmospheric
Chemistry
and Physics
Discussions

(CO_2) in terms of total radiative forcing, CH_4 can account for 20% of recent trends in global surface air temperatures, which have risen approximately 0.6 K over the past century (Kirschke et al., 2013; Ciais et al., 2014). Since emissions of CH_4 from wetlands represent ∼30% of the global CH_4 produced annually, it is of critical scientific interest to determine whether these sources will strengthen in a warming climate (Whalen, 2005; Kirschke et al., 2013; Ciais et al., 2014). In particular, it has

5   been speculated that increased air temperatures in wetlands north of 40N, combined with ecological, hydrological, and bio-geochemical changes could couple into a temperature-emissions feedback, potentially leading to a depletion of organic carbon previously sequestered in below-ground permafrost and increased atmospheric CH_4 (Schuur et al., 2015; Tarnocai et al., 2009).

Temperature increases have been more drastic in Arctic regions, which have seen almost 3 K increases in air temperatures since the beginning of the 20th century (Overland et al., 2015), with 1.8 K occurring over the past three decades (Collins

10   et al., 2013). Rising air surface temperatures have resulted in a response in soil temperatures, with winter-time observations of permafrost core temperatures in Alaska showing increases of approximately 3–4 K on the Arctic Coastal Plain of Alaska at borehole depths of 5–20 m and 1–2 K in the Brooks Range at depths of 20 m (Osterkamp, 2005). If current Arctic climate trends continue, up to 10–30% of permafrost in Arctic lowlands could significantly degrade, leading to measurable ecological shifts and adding new labile organic carbon to the carbon cycle (Jorgenson et al., 2006).

15   From a biogeochemical perspective, CH_4 is produced in soils below the water table, which provide the anaerobic conditions necessary for fermentation of soil organic carbon stocks (Whalen, 2005). The fermented organic carbon products are then consumed by methanogenic archaea within the soil column, producing CH_4 gas (Whalen, 2005). As CH_4 production is a biological process relying on microbial activity, it is commonly observed that high CH_4 emissions are coincident with warm, wetland soils (Sturtevant et al., 2012; Olefeldt et al., 2013; Kirschke et al., 2013; Christensen, 1993).

20   In Alaska and the neighbouring Yukon, seasonal wetlands make up nearly 12% of the total surface area (Bergamaschi et al., 2007), with 92% of soils within continuous permafrost zone (Hugelius et al., 2013). Since Alaska is frozen most of the year, its carbon stocks have long been preserved within permafrost, limiting carbon mobilization through respiration. In spite of recent warming and mobilization of sequestered carbon, a recent study of atmospheric mole fractions of CH_4 in the North Slope of Alaska found no significant increase in CH_4 emissions over the past 29 years (Sweeney et al., 2016). Field observations have

25   also reported that microbial communities linked to CH_4 oxidation thrive in soils with low moisture content (Xue et al., 2016), highlighting that a warming climate may not have a one-to-one effect on biogenic CH_4 flux at a regional scale.

Numerous past studies have been conducted in permafrost regions such as Alaska at the scale of chambers (as summarized by Olefeldt et al., 2013) and eddy-covariance towers (e.g. Fan et al., 1992; Sturtevant et al., 2012; Zona et al., 2016), providing insight on factors controlling CH_4 emissions at the scale of ∼1 m to ∼1 km. These studies have revealed that CH_4 emissions

30   are spatially inhomogeneous at those scales and are highly dependent on local conditions such as soil moisture, temperature, elevation and soil carbon. While these process-based studies are extremely important, extrapolating the results to larger scales can be challenging. At the other extreme, top-down inversion studies estimate global CH_4 emissions using measurements from surface sites around the world and/or satellite observations coupled to sophisticated transport models (Bruhwiler et al., 2014; Bergamaschi et al., 2013; Chen and Prinn, 2006). These results provide insight on regional emissions; however, it is more

35   difficult to understand local drivers that affect emission rates. More recently, tall towers, either alone or in a network, and

aircraft observations, have been used to study regional emissions of CH_4 from permafrost areas (Karion et al., 2016; Sasakawa et al., 2010; Chang et al., 2014). Tall towers are advantageous since their operation is less dependent on weather conditions than static chamber measurements, they provide continuous measurements and their footprint spans a much larger area than a typical eddy-covariance tower. Despite this, in a region like Alaska, where high mountains significantly affect transport

5   patterns, a single tower may not be sensitive to the entire region throughout the year (Karion et al., 2016). In contrast, aircraft observations, by virtue of their mobile platform, can sample larger regions and can periodically measure in the free troposphere to establish background levels. However, their coverage is dependent on weather conditions.

   In this study, we estimate surface CH_4 fluxes using in situ observations of CH_4 from an aircraft that flew in Alaska as part of the Carbon in Arctic Reservoirs Vulnerability Experiment (CARVE). This work uses similar methods as Chang et al. (2014),

10   but extends the analysis to include the growing seasons of 2013 and 2014 and explores how their interannual and intra-annual variability can be explained by hydrological and environmental controls at a regional scale. A recent study by Miller et al. (2016) explores similar questions using a more complex geostatistical inversion model constrained by a much larger data set. Using simple multiple linear regression models, we investigate the relationship between land surface properties and observed atmospheric CH_4 and find that the results are similar. This could provide a simpler diagnostic tool for regional carbon cycle

15   analysis.

2   Methods

2.1   Description of aircraft flights

The data presented in this study were collected on board a National Aeronautics and Space Agency (NASA) C23-B aircraft during the Alaskan growing seasons of 2012–2014. In 2012, flights occurred in the last two weeks of each month from May

20   to September for a total of 31 flight days and 212 flight hours. In 2013 and 2014, flights occurred in the first two weeks of each month from April to October and May to November, resulting in 290 and 300 flight hours over 42 and 48 flight days, respectively. All flights analyzed in this study originated from Fairbanks, AK and stayed within Alaska. Not all regions and altitudes were sampled every month since the flight routes were limited by icing concerns and weather conditions. Data were typically acquired at 150 m above ground level (AGL) to maximize sensitivity to local surface-atmosphere fluxes; however,

25   periodic profiling of the atmosphere to 5–6 km AGL occurred throughout the flights to characterize planetary boundary layer height and mole fractions in the free troposphere.

2.2   Measurements

Mole fractions of CH_4, CO_2, carbon monoxide (CO) and water vapour (H_2O) were measured in situ every ~2.5 s using two independent cavity ring-down spectrometers. Each system had an individual rear-facing inlet on the port side of the

30   aircraft. Sample flow from the inlets passed through a length of Synflex tubing with an approximate transit time of 30 ± 2s. The first system (Picarro; G1301-m in 2012, G2401-m in 2013 and 2014) directly sampled the air without any pre-treatment and

alternately sampled from one of two on-board calibration cylinders every 30 min. These on-board calibration cylinders were changed throughout the campaigns as the pressure approached 3.4 MPa (500 psi). They were calibrated by NOAA before and after each deployment. Calibration for the water vapour correction was conducted on the flight instrument before and after each year's campaign according to Chen et al. (2010). Further details of this system can be found in Karion et al. (2013).

5　　The sample flow in the second system first passed through a 0.2 μm Teflon filter before passing through a Nafion dryer followed by a dry ice trap which effectively lowered the dewpoint temperature of the sample flow to ∼195K before entering the spectrometer (Picarro; G2401-m). This reduced the water vapour of the sample flow to $< 0.001\%$ and allowed dry mole fractions of CH_4, CO_2 and CO to be directly measured. Two onboard 8 L calibration cylinders (independent of the first system's) were sampled at the beginning and end of every flight as well as every 30 min during flight. These in-flight calibrations

10　were linearly interpolated between calibration times, which were then additionally interpolated to calculate the measured mole fraction in between calibrations. In-flight calibrations that were greater than 2.5 standard deviations away from the mean of the calibrations for a given flight were excluded.

　　　Before each year's campaign, the onboard calibration cylinders for the second system were flushed twice and then filled from 30 L fill tanks (Scott Marrin). Due to the longer sampling seasons in 2013 and 2014, the onboard calibration tanks were topped

15　up once in each of those years with the original fill tanks before the pressure dropped below 3.4 MPa. Both the original fill tanks from Scott Marrin and the onboard calibration cylinders were calibrated in the laboratory with the spectrometer used in flight before and after each year's campaign using tanks with known mole fractions obtained from NOAA, tying our measurements to the WMO scales (Dlugokencky et al., 2005; Novelli et al., 1994; Zhao and Tans, 2006). The differences in mole fractions before and after each year's flight campaigns in both the on-board calibration cylinder and the fill tanks were less than 0.15

20　ppm for CO_2, 0.8 ppb for CH_4 and 7 ppb for CO, all of which were within the precision of the system. The mole fraction in the on-board calibration cylinders was therefore treated as constant throughout each year's study and assumed to be unaffected by the addition of gas. It was also assumed that any changes within any of the tanks were negligible throughout each year's campaign.

　　　The one deviation was that the onboard calibration cylinders were not calibrated before the 2012 deployment due to time

25　constraints. However, these cylinders were calibrated after the 2012 campaign and compared to the fill tanks calibrated before and after that year's campaign. Except for CO_2 in one of the onboard calibration cylinders, which was 0.29 ppm lower than the fill tank, the comparison with the fill tanks for the other gases all fell into the ranges given above. In the case of this exception, the post-mission calibration of the onboard calibration cylinder was used since the tank was not topped up during that year's mission.

30　　Comparison of the two systems showed a mean difference of 0.8, 0.3 and 0.4 ppb for CH_4 for 2012–2014, respectively with no dependence on water vapour levels ($r^2 = 0.008$). The mole fractions presented in this study merges those measured by both systems, to fill in times when one of the systems was calibrating or functioning imperfectly. The system used to gap-fill is offset by the mean difference between the two systems for a given flight. Since our analysis is based on the difference between mole fractions in the free troposphere and the mixed layer (see below), this treatment does not bias our analysis. The greenhouse

35　gas measurements were merged to a common 5 s time scale along with the location data, measured using a global positioning

Atmospheric
Chemistry
and Physics
Discussions

unit (GPS) (Crossbow; NAV420); outside air pressure (Parascientific; 745-15A); outside air temperature (Harco; 100366-18), dewpoint temperature (Edgetech; Vigilant) and ozone (2B Technologies; 205).

3 Analysis methods

3.1 Footprint sensitivity

To relate the variation of observed mole fractions of CH_4 to surface processes, an adjoint atmospheric transport model was used to simulate the sensitivity of the air parcels measured by the aircraft to the surface influence. Specifically, the Weather Research and Forecasting (WRF; Skamarock et al. (2008)) regional numerical weather prediction model was coupled offline to the Stochastic Time-Inverted Lagrangian Transport model (STILT; Lin et al. (2003)). The coupling of the STILT model with WRF meteorological fields, hereafter WRF-STILT, is described by Nehrkorn et al. (2010) The polar variant of WRF (Hines et al., 2011; Bromwich et al., 2009; Hines and Bromwich, 2008) coupled with STILT was configured for the Arctic CARVE domain by Henderson et al. (2015), who provide a detailed description and meteorological validation of the high-resolution simulations performed on a 3.3-km grid suitable for simulating particle transport on regional scales in mountainous terrain. Their initial STILT footprints from WRF v3.4.1 were used in the analysis of Chang et al. (2014). The current investigation uses WRF v3.5.1 and incorporates recently-available PIOMAS cryosphere fields (Zhang and Rothrock, 2003; Hines et al., 2015) and footprints on an expanded circumpolar domain north of 30N, among other methodological improvements.

To derive source-receptor relationships, each STILT simulation launched 500 particles into the atmosphere at the location of a measurement and traced its dispersion through the atmosphere in reverse time over 10 days via stochastic (i.e. random/probabilistic) processes determined from the underlying meteorology (Lin et al., 2003; Henderson et al., 2015). At every one-hour time step, particles that are in the lower half of the boundary layer are assumed to be influenced by the surface and are gridded to generate a footprint sensitivity plot. The footprint used in this analysis was calculated on a $0.5° \times 0.5°$ lat/lon grid. The unit of the footprints is abundance flux^{-1} (e.g. ppb (nmol m^{-2}s^{-1})$^{-1}$, where ppb is parts per billion) (Lin et al., 2003) and allows us to relate surface emissions to an observation at a given time and location.

To avoid unnecessary computational costs, the measurement locations were first placed into discrete bins on a grid of 5 km in the horizontal, 50 m in the vertical below 1 km and 100 m in the vertical above 1 km (Chang et al., 2014). Measurement times were also rounded to the hour to match the time resolution of the meteorological fields. The use of WRF at high resolution to drive the STILT model results in higher fidelity meteorological fields and subsequent transport calculations than afforded by most global reanalysis (Nehrkorn et al., 2010; Henderson et al., 2015).

3.2 Domain

This analysis focuses on the influence of surface emissions from Alaska and Yukon on observed CH_4 mole fractions. To this end, we restricted our region of interest to 50–75N and 130–170W (Fig. 1) and only consider footprint sensitivity derived from WRF-STILT during the first five days preceding each receptor point. The time-scale of five days was chosen under the

Atmospheric
Chemistry
and Physics
Discussions

assumption that sources outside the domain would have transport timescales roughly equal to that of free-tropospheric mixing and would therefore only contribute to background values of CH_4. Figure 2 shows the cumulative 5 day footprint of our analyzed times for each year averaged over the number of profiles in each year, and shows that our observations are most influenced by the boreal interior of Alaska as well as tundra regions. It should be noted that although our mean footprints were

5   more sensitive to the North Slope of Alaska in 2012, our absolute sensitivity was comparable in all three years due to the increased number of flights in 2013 and 2014.

Our choice of spatial domain was determined by the distribution in five-day footprint. As will be defined in the subsequent section concerning the mixed layer, footprint sensitivity simulations that had less than 1.0 ppb (nmol m^{-2} s^{-1})$^{-1}$ total land sensitivity were identified as being in the free troposphere, following Henderson et al. (2015). For an idealized homogeneous

10   distribution of sensitivity, where an air parcel is equally sensitive to all land areas within the domain, this threshold would translate to ~1×10^{-4} ppb (nmol m^{-2} s^{-1})$^{-1}$ in any given grid cell. It was assumed that areas of the globe with sensitivities smaller than this threshold did not significantly contribute to CH_4 enhancements, since, even at extreme fluxes of 1000 mg m^{-2} d^{-1}, they would contribute <0.1 ppb to the observed enhancement. In the cumulative 5 day footprints shown in Fig. 2, 71.2% of the footprint that exceeded the grid-cell threshold was from land in the domain of choice, while 28.5% could be

15   sourced to oceans. It is worth noting that the previous study of Chang et al. (2014) restricted their domain to 135°W. While the May–September footprints showed that <2% of the footprint originated in regions east of 135°W, it was found that at least 5% of the total land sensitivity in April, October, and November came from the Canadian Yukon. Of all the land surface influence on our observations, only 0.3% originated from land outside of our study region, suggesting that our sampling strategy and choice of domain allowed our observations to be most sensitive to surface emissions from the study region.

20   ## 3.3   Mixed layer

We use the term 'mixed layer' to refer to the combination of both the residual layer and the boundary layer throughout the remainder of this paper. As our footprint sensitivity predicts that we are sensitive to surface fluxes 5 days previous to measurement, quantifying the total amount of CH_4 emitted requires calculating the amount of CH_4 in both the boundary layer and the residual layers from previous days. By determining the altitude at which the residual layer is capped, it is possible to determine

25   the portion of a vertical profile that is affected by surface emissions versus the portion that represents background levels in the free troposphere. The CH_4 column enhancement within the mixed layer will be used in Sect. 3.4 to estimate CH_4 emissions.

We estimate the bottom of the free troposphere (h) by calculating the refractivity (N) using parameters measured at different altitudes on the aircraft (Chan and Wood, 2013; Bean and Dutton, 1966):

$$N = 77.6\frac{P}{T} + 3.77 \cdot 10^5 \frac{P_w}{T^2}, \tag{1}$$

30   where P and P_w are the atmospheric pressure of air and water in hPa, respectively, and T is the atmospheric temperature in K. The height at the minimum of the gradient in N is the top of the mixed layer.

In analyzing individual profiles it was often found that this method over-estimated the boundary layer height as compared to profiles of CH_4, O_3 and the total land surface sensitivity calculated by WRF-STILT; as a secondary calculation, the height

at which WRF-STILT sensitivities dropped below 1.0 ppb (nmol m^{-2} s^{-1})$^{-1}$ was used to approximate h (Henderson et al., 2015). Upon individual inspection of profiles it was found that in 25% of cases (i.e. 68 profiles) neither method captured an h which correctly separated the free troposphere and mixed layer. After removing these profiles, a further 25% of profiles within the remaining set (i.e. 50) had h differing by >750 m between the two methods (paired t-test; p<0.005). In these cases, either

5   the boundary layer dynamics within WRF-STILT were not representative of local meteorology or there was too much variance about the minimum of the gradient in N. Therefore, these profiles were not included in the analysis. In the final set of profiles used for analysis, a paired t-test found that the two methods did not statistically differ from each other (p>0.1) and both agreed to within 500 m ∼90% (r^2 = 0.6) of the time. We attempted to use other variables such as virtual potential temperature to define the mixed layer but the methods described above gave the most consistent results.

10   Across all years h was found to occur between 1.1 and 1.8 km with a median of 1.5 km above Alaska, consistent with estimates derived from satellite retrievals (Chan and Wood, 2013). On average, h in May–September was 30% higher than in April, October or November. These findings are consistent with lower solar zenith angles and shorter solar days in colder months, both of which reduce the strength of convective forces which form the boundary layer (Stull, 1988).

3.4   CH$_4$ flux estimates

15   In this analysis, we use column enhancements of CH$_4$ (ΔCH$_4$) to estimate surface fluxes (Chang et al., 2014; Gatti et al., 2014; Chou et al., 2002). This method assumes that CH$_4$ enhancements below h that are above background levels are a result of interactions with the local surface that are not well-mixed with the free troposphere. Surface fluxes are determined by calculating the corresponding surface influence throughout the column using the footprint sensitivities determined from WRF-STILT. This method of calculating ΔCH$_4$ is less reliant on the accurate simulation of the vertical structure of the atmosphere as

20   well as turbulent transport in the lower atmosphere. Instead, we rely on the integrated model simulation to match the integrated observations.

To calculate ΔCH$_4$, measurements in a vertical profile were first block-averaged by altitude into 250 m bins. A sample of such a profile observed during the CARVE campaign is shown in Fig. 3 and shows median, minimum and maximum [CH$_4$] observed in each 250 m bin up to 3 km along with the estimated ΔCH$_4$ from the WRF-STILT footprint influence according to

25   Eq. 3. In this case the calculation of the refractive index (N) properly captured the transition from the mixed layer to the free troposphere and WRF-STILT adequately modelled the mixed layer, leading to a reasonable estimate of CH$_4$ flux. Using h as the upper bound on the section of the profile affected by local sources and sinks:

$$\Delta\text{CH}_4 = \int\limits_0^h ([\text{CH}_4](z) - [\text{CH}_4]_0) \frac{P_d(z)}{R^* T(z)} dz, \tag{2}$$

where ΔCH$_4$ is the column enhancement in the mixed layer of CH$_4$ in (ppb), [CH$_4$]$_0$ is the estimated background of CH$_4$

30   in the free troposphere averaged in the first kilometer above h, P_d is the calculated atmospheric pressure of dry air using measurements of P and P_w, R^* is the universal gas constant, and z is the height above ground level (AGL) as calculated from the height above sea level measured by the GPS and an underlying digital elevation map within the input meteorology of WRF.

Atmospheric
Chemistry
and Physics
Discussions

As an entrainment zone was usually evident in profiles of CH_4, where mixing ratios were between free troposphere and mixed layer values, 500 m was added to mixing layer height in order to estimate $[CH_4]_0$. Since $[CH_4]_0$ is stable with altitude in the free troposphere, this should not affect the integral in Eq. 2.

A similar calculation was undertaken for the corresponding footprint sensitivity to calculate the sensitivity of the mixed layer to the total surface (ΔI with units of ppb (nmol m^{-2} s^{-1})$^{-1}$). As a first estimate, our a priori CH_4 flux is assumed to be uniformly emitting over our entire domain. Footprint sensitivities were restricted to the study domain and masked from seas and mountains, which we assume to be neither sources nor sinks of atmospheric CH_4 and therefore did not contribute to ΔCH_4. The total mixed layer sensitivity, ΔI, is then scaled to match ΔCH_4. This scaling factor is the CH_4 flux estimate, $\hat{E}$:

$$\hat{E} = \frac{\Delta CH_4}{\Delta I}, \tag{3}$$

with appropriate unit conversion to mg CH_4 m^{-2} d^{-1}.

Monthly mean CH_4 flux ($\overline{E}$) were estimated by weighing individual flux estimates by the total footprint sensitivity of each profile (Chang et al., 2014; Karion et al., 2016), so that:

$$\overline{E} = \frac{(\sum \hat{E} \times \Delta I)}{\sum \Delta I} = \frac{\sum \Delta CH_4}{\sum \Delta I}. \tag{4}$$

This allowed profiles with larger spatial coverage to be more represented while profiles with lower ΔI, which sometimes resulted in a high $\hat{E}$, did not inadvertently skew the mean estimate.

Growing season budgets were calculated by integrating the monthly emissions from May through September and over our study domain (excluding mountains). Uncertainties in this budget are estimated using the standard error calculated from the weighted standard deviations in the monthly means. The surface area of our domain was estimated using a digital elevation map from the Advanced Spaceborne Thermal Emission and Reflection Radiometer (ASTER) to estimate the enhancement of surface area in sloped terrain (Jenness, 2004). A land/ocean mask at 0.1°x0.1° was then used to approximate the fraction of land cover at 0.5°x0.5° to estimate surface area in coastal grid cells (i.e. $A_{land} = A^* f_{land}$). The total land surface area of our domain is estimated to be 2.1 million km^2 including mountains and 1.04 million km^2 without.

To ensure that our CH_4 flux estimates were not affected by combustion, measurements of CO were used as an atmospheric tracer for air influenced by biomass burning events or oil development off-gassing, which co-emit CO and CH_4. Any profile which had measurements of CO exceeding 150 ppb within the mixed layer were not used in the analysis. This threshold was determined by observing that the annual distribution of CO deviates from normal above 150 ppb (Chang et al., 2014). After CO screening, each individual vertical profile was assessed on a case-by-case basis to ensure that the WRF-STILT model had adequately captured a mixed layer, i.e. the footprint sensitivity attenuated to zero as altitude increased and that the estimated mixed layer height from WRF-STILT clearly separated the mixed layer from the free troposphere. In general, if h defined by WRF-STILT was below 500 m, the profile was rejected due to difficulty in calculating the column enhancement since there was only one binned point below h. Of the 273 profiles identified, 9 were rejected due to excessive CO mole fractions, 68 were rejected due to a poor separation of the mixed layer and the free troposphere, and a further 50 were rejected when h differed by more than 750 m using the two methods described in Sect. 3.3. The remaining 146 profiles, just under half of all the

profiles, were kept for analysis. While this is a severe reduction in data, footprint sensitivity plots comparing the total footprint sensitivity of all the receptor points within all profiles against the total footprint sensitivity of those within the profiles kept for analysis showed no significant bias. As a result, this subset is thought to be both representative of the CARVE sampling campaign and free from errors in integration limits.

3.5   Eco-region dynamics

The previous assumption that the study region emits CH_4 uniformly is correct only to the zeroth-order and serves only as the best estimate for the total magnitude of flux. However, this assumption misses much of the spatiotemporal heterogeneity observed in emissions across and even within different biological and hydrological regimes (as summarized by Olefeldt et al., 2013). At regional scales, such as in this study, it is useful to separate the domain into eco-regions which group regions with similar vegetation, elevation, soil type and hydrologic flow. One can then use the different eco-regions as a basis set of independent sources and sinks in a linear inversion. The eco-regions used within this study were taken from the Environmental Protection Agencies (EPA) Level II map of eco-regions and grouped into the three following land types: tundra, which includes 'Alaska Tundra'; boreal, which includes 'Alaska Boreal Interior', and 'Taiga Cordillera'; and mountains, which includes 'Brooks Range Tundra', 'Marine West Coast Forest', and 'Boreal Cordillera' (Commission for Environmental Cooperation, 1997) (see Fig. 1). While 'Marine West Coast Forests' are not mountainous by definition, a study of CH_4 fluxes north of 50°N identified heavily forested areas as being negligible sinks of CH_4 (Olefeldt et al., 2013). Therefore these forests are suitably grouped with mountains under the assumption that footprint sensitivity from these areas did not affect observed ΔCH_4.

By calculating the mean fraction of the influence of each eco-region on our measurements using the footprint sensitivity maps, it is possible to estimate the CH_4 flux from each eco-region using multiple linear least-squares regression according to the following:

$$\hat{E} = \sum_i f_i E_i, \tag{5}$$

where f_i are the fractions of influence from different eco-regions, $\hat{E}$ are the uniform CH_4 flux estimates, and E_i are the CH_4 fluxes from each eco-region. These estimates were grouped by month across all three years to maintain a sufficient sample size. To test the assumption that emissions from the mountain land type negligibly affected ΔCH_4, CH_4 flux was estimated with and without the mountain land type and presented in Sect. 4.4.2.

3.6   Regression analysis

To explore how the variability in CH_4 flux estimates is related to ecological, biological and hydrological parameters, the footprint sensitivity functions were also used to calculate weighted means of different variables common in process-based models of CH_4 flux. Maps that were included in this analysis were: surface, 10-cm and 40-cm daily soil temperature (T_x, where x is the depth [K]) and liquid soil moisture content (S_x [-]) from the North American Regional Reanalysis (NARR)

Atmospheric
Chemistry
and Physics
Discussions

project; digital elevation (z [m]) from ASTER; days since thaw (DST), derived from passive microwave satellite observations of surface thaw (Steiner et al., 2015); wetlands (%) (Bergamaschi et al., 2007); 30-cm and 100-cm soil organic carbon content (C_x, kg/m^2) from the Northern Circumpolar Soil Carbon Database (NCSCD) (Hugelius et al., 2013); and percent of soils classed as turbels, histels, gelisols or non-soils from NCSCD (Hugelius et al., 2013).

5   Previous correlation analyses have suggested that CH$_4$ flux varies non-linearly with variables such as soil temperature (Yvon-Durocher et al., 2014) and elevation (Karion et al., 2016). As such, the following functional forms were used to characterize variability in CH$_4$ flux:

$$E = e^{f(x)} \tag{6}$$

$$f(x) = \begin{cases} E_a \left(\frac{1}{k\overline{x}} - \frac{1}{kx} \right), & \text{Boltzmann-Arrhenius-Type} \\ \left(\frac{1}{x+\overline{x}} \right), & \text{Inverse-Type} \\ (x - \overline{x}), & \text{Linear-Type} \end{cases} \tag{7}$$

10   where E is CH$_4$ flux, x is a hypothesized predictor variable, eV is the value of an electron volt in Joules (1.602x10^{-19} J), k is the Boltzmann constant (1.38x10^{-23} J/K), and $\overline{x}$ represents the mean sampled value of x. This transformation of units is performed such that when the predictor variable is soil temperature, the fitted parameter optimizes the activation energy (E$_a$) in units of eV (Yvon-Durocher et al., 2014).

Multi-variable fits were also performed using an equation of the form:

15    $$\hat{E} = e^{f(Z)\hat{\beta}}, \tag{8}$$

where $\hat{E}$ is an Nx1 vector of modelled CH$_4$ flux estimates, Z is an Nx(M+1) matrix with M columns of predictor variables transformed by $f(x)$ and one column of ones, and $\hat{\beta}$ is an (M+1)x1 vector of estimated parameters. We searched through all possible combinations of functional forms by allowing the M columns of Z to take either the Boltzmann-Arrhenius, inverse, or linear forms written in Eq. 7, leaving the column of ones to fit a constant. The parameter vector $\hat{\beta}$ is then constrained using
20   the Levenberg-Marquardt algorithm for non-linear least-squares regression. Subsets of the data (n<N) were also fit to explore behaviour in limiting spatial and temporal cases. The best fit for each subset was chosen if it minimized the Aikake Information Criterion (AIC) (Burnham et al., 2011).

Since our estimates represent 5 day averages of CH$_4$ flux (see Sect. 3.1 & 3.4), flux estimates from nearby days can be significantly correlated. To compensate for this correlation, CH$_4$ flux estimates were first averaged into 5-day bins before fitting
25   to reduce issues of autocorrelation and to generate independent estimates of CH$_4$ flux. As with the monthly mean estimates, these were weighted by the total footprint influence. This temporal averaging reduced the total number of independent estimates used in the regression from 146 to 68.

4 Results & discussion

In the following sections, we present estimates of regionally averaged monthly CH_4 flux and the net total CH_4 emitted from our study domain from May–September. A discussion of the source of uncertainties in determining $[CH_4]_0$ will follow. Finally, the set of CH_4 fluxes estimated across 2012–2014 will be used to motivate discussions of how sampling different eco-regions

5 across a dynamic range of soil conditions (e.g. soil temperature, soil moisture, soil type) affected the estimated CH_4 flux and budget.

4.1 CH_4 flux estimates

Using the methods described in Sect. 3.4, monthly mean CH_4 fluxes for 2012–2014 were estimated from individual aircraft profiles of the atmosphere (Fig. 4). As will be shown in Sect. 4.4, we found that footprint sensitivity from oceans and mountains

10 were poorly correlated with observations of ΔCH_4. Therefore the estimated fluxes presented in this subsection only represent CH_4 flux from the boreal and tundra eco-regions defined in Sect. 3.5. These estimates ranged from 2–36 mg CH_4 m^{-2} d^{-1} (95% C.I.) for individual profiles and showed a distinct seasonal cycle that peaked in late July or early August across all years, consistent with tall and eddy-covariance tower studies (e.g. Karion et al., 2016; Zona et al., 2016; Sweeney et al., 2016). Additionally, they provide observational evidence that region-wide CH_4 flux may on average be as high as 5 mg m^{-2} d^{-1} in

15 the colder months of April and November, also consistent with previous studies on the North Slope (Zona et al., 2016) and interior (Karion et al., 2016) of Alaska.

Monthly mean flux estimates were found to be higher than those inferred from the CRV tower near Fairbanks for the same months (3–9 mg CH_4 m^{-2} d^{-1}) (Karion et al., 2016), although the ranges from the two studies overlap. As discussed by Karion et al. (2016), the tower observations likely underestimate CH_4 flux compared to the aircraft observations because of

20 the aircraft's increased sensitivity to the North Slope and southwestern Alaska, regions that are known to be seasonal wetlands (and therefore a significant CH_4 source (Bergamaschi et al., 2007)), as compared to the interior sites which were more sensitive to upland regions that are thought to emit less CH_4 (Olefeldt et al., 2013).

4.2 CH_4 budget calculations

Integrating over the months sampled every year (May–September), we estimate CH_4 emissions from our study region to be

25 2.1 ± 0.5 Tg, 1.7 ± 0.4 Tg and 2.0 ± 0.3 Tg for 2012–2014, respectively, with the assumption that all land surfaces (excluding mountains) emit at a uniform rate over the entire month. As our observations do not extend throughout the colder months, we do not provide annual budget estimates since other studies have found that significant emissions of CH_4 are observed in the shoulder and cold seasons (Zona et al., 2016; Sweeney et al., 2016; Karion et al., 2016).

Previous estimates of emissions from Alaska during the growing season include the study by Chang et al. (2014), who used

30 a similar method to estimate the May–September 2012 emissions to be 2.1 ± 0.5 Tg, as well as the geostatistical inversion of the CARVE observations by Miller et al. (2016), who estimated May–October CH_4 emissions of 1.80 ± 0.45, 1.65 ± 0.43 and 1.77 ± 0.45 Tg CH_4 for 2012–2014, respectively. Our mean estimates are within the uncertainties of these other studies,

Atmospheric
Chemistry
and Physics
Discussions

especially when we account for the $\sim$20% greater area in our study domain. It is promising that our relatively simple method for calculating budgets using selected profiles from the CARVE aircraft observations arrives at similar estimates to values derived from the much more complex geostatistical inverse model used by Miller et al. (2016), particularly as their study was constrained by all the aircraft observations as well as hourly averaged observations from the CRV tower.

5   Our estimates of May–September CH_4 flux, have a mean of 2.0 ± 0.4 Tg, and show no significant difference over the three years. These results are consistent with the findings reported by Miller et al. (2016), who suggest that regional CH_4 emissions would require decades to respond to changes in surface conditions. Similarly, a recent analysis of long-term measurements of CH_4 flux on the North Slope in Alaska observed little change in boundary layer CH_4 enhancement over the past 29 years, despite increases in air temperature (Sweeney et al., 2016). This lack of trend could potentially be related to methanogen

10 community structure in the Arctic as recent microbiological research has found that communities from Arctic soils that were incubated at lower temperatures were insensitive to substrate manipulations, indicating that Arctic methanogens may not be sensitive to the addition of new labile carbon from thawing permafrost (Blake et al., 2015). While it is true that local-scale permafrost degradation patterns such as thermokarsts can result in local CH_4 fluxes of >100 mg m^{-2} d^{-1} (Johnston et al., 2014), multi-decadal studies such as Sweeney et al. (2016) suggest that at a regional scale, CH_4 fluxes in Alaska have been

15 stable.

4.3 CH_4 background estimates

4.3.1   Comparison of background CH_4

Since our calculations of ΔCH_4 rely on the free tropospheric $[CH_4]$ to represent background $[CH_4]$ in the mixed layer, it is important to demonstrate that these values are comparable. As seen in Fig. 5, a distinct seasonal cycle in $[CH_4]_0$ is evident and

20 is consistent with cycles observed in the NOAA Global CH_4 Network (Dlugogencky, 2016). This gives us confidence that our calculated $[CH_4]_0$ is not strongly affected by changes in circulation due to long range transport or stratospheric intrusion of clean air.

To assess the accuracy of our estimates of $[CH_4]_0$, we compare our values to in situ observations of boundary layer CH_4 background observed at the Barrow Observatory ground station (BRW: 71.3°N, 156.6°W) in 2013 and 2014 (Dlugogencky,

25 2016). Because the station did not measure $[CH_4]$ in 2012 (Sweeney et al., 2016), we instead compared the 2012 CARVE $[CH_4]_0$ estimates to the free tropospheric backgrounds measured monthly at the Poker Flats site in interior Alaska (Global Monitoring Division, 2016). We also compared our estimate of $[CH_4]_0$ to the backgrounds determined for the CRV tower (Karion et al., 2016). These other estimates of CH_4 background levels were generally within the standard deviation of $[CH_4]_0$ estimated from the CARVE profiles ($\pm$8 ppb in 2012 and $\pm$6 ppb in 2013 and 2014). The exceptions were August 2013 and

30 May 2014 when the CARVE observations were lower than the boundary layer CH_4 background observed at BRW, possibly resulting in an overestimation of CH_4 flux. It should be noted that the BRW site is located on the northern shore of Alaska and is separated from the Alaskan interior by the Brooks Range so it is not always influenced by the same air mass that affects the remainder of the study region. While the backgrounds estimated from the CRV tower for August 2013 are within our variability,

the May 2014 background estimate is between our estimate and the levels observed at BRW. To evaluate the magnitude of this effect on the estimated May–September budgets, the CH_4 flux using the BRW ground station observations were calculated for those two months. Resulting May–September budgets using these new values are 1.5±0.2 and 1.8±0.4 Tg CH_4 for 2013 and 2014, respectively. Since these values are within the uncertainties of our initial budget estimates and our background estimates

5 correspond to those from the CRV tower, we believe that our estimates of $[CH_4]_0$ are representative of background levels in the mixed layer.

4.3.2 CH_4 background growth rate

Across the entire campaign, the estimated $[CH_4]_0$ had a median and standard deviation of 1880 ± 20 ppb, and a distinct seasonal cycle with higher mole fractions in colder months than in warmer months (Fig. 5). This cycle is chemically driven

10 and is consistent with observations from global $[CH_4]$ observations (Dlugogencky, 2016). From Fig. 5, it is also evident that background CH_4 in the free troposphere rose from 2012–2014.

We estimate the atmospheric growth rate using monthly mean CARVE observed $[CH_4]_0$ fit to the function $y = \sum_{k=0}^{1} \sin(2\pi t + \frac{k\pi}{2}) + \sum_{k=0}^{1} t^k$, where time ($t$) is in units of years. This function is a simplified form of the function used by NOAA to estimate the global growth rate of CH_4 from their observation network (ESRL, 2016). Fitting with the Levenberg-Marquadt algorithm

15 for non-linear least-squares, we estimate the atmospheric growth rate in the free troposphere over Alaska to be 9 ± 2 ppb/yr (p<0.001) with a coefficient of determination of 0.77. The estimated growth rate is consistent with the 9 ± 1 ppb/yr and 8.6 ± 0.6 ppb/yr observed at Barrow (11 m a.s.l.) and Mauna Loa, HI (3397 m a.s.l.) respectively.

Overall we find that the monthly mean and annual growth rate determined from CARVE was the same as BRW within the variability of our observations, with the exception of a few months. These results indicate that local mixed layer $[CH_4]_0$ in

20 Alaska can be constrained from free tropospheric measurements and gives us confidence in our estimates of ΔCH_4.

4.4 Eco-region Dynamics

4.4.1 Tundra & Boreal Eco-regions

Figure 6 shows the monthly emissions estimated for the tundra and boreal eco-regions over all three years estimated using the linear system in Eq. 5. The seasonal average CH_4 flux from tundra regions was 21 ± 3 mg m^{-2} d^{-1} and ranged from 6–34

25 mg m^{-2} d^{-1}. Although comparable, our mean is lower and our range is narrower than those reported in a database of flux observations at the chamber-scale compiled by Olefeldt et al. (2013), who found that average CH_4 flux from wet tundra north of 50 N was 64.5 mg m^{-2} d^{-1} and ranged between 31.9 and 100.6 mg m^{-2} d^{-1}. This is likely a result of our estimation method, which relies on a large degree of spatial and temporal averaging which smooths out the high CH_4 bursts that can be captured by flux chambers. Our estimates are also comparable to flux observations in 2013–2014 from eddy-covariance towers

30 on the North Slope, where the monthly mean emissions from May to September ranged from 6–21 mg m^{-2} d^{-1} (Zona et al., 2016), as well as from the Yukon River Delta (25 mg m^{-2} d^{-1}) (Fan et al., 1992).

The mean monthly flux was much lower from boreal regions. On average it was 10 ± 2 mg m^{-2} d^{-1}, and ranged from $4 - 21$ mg m^{-2} d^{-1}. The database by Olefeldt et al. (2013) variously classified areas within the boreal region as bogs, fens and palsas, which emit on average $7 - 37$ mg CH$_4$ m^{-2} d^{-1} (Olefeldt et al., 2013). An additional study, which made flux measurements using an eddy covariance tower within a poorly drained forested region in Alaska, found that CH$_4$ flux varied from $3 - 11$ mg m^{-2} d^{-1} in the wettest regions (Iwata et al., 2015). Again, as with the tundra ecosystem, our spatial and temporal averaging method will smooth any CH$_4$ bursts.

Considering the period of May–September, the total flux from both ecosystems (2.2 ± 0.2 Tg) was consistent with the mean of the net budget calculated in the previous section assuming the ecosystems were identical. This analysis also estimates that the tundra eco-region, which represented 18% of the total study area, accounted for more than half of the total flux. Nevertheless, emissions from boreal regions cannot be neglected in estimates of the regional budget since their spatial coverage is quite extensive.

In Fig. 6, emissions from boreal regions appear to lag tundra regions by one month. This offset could be due to a more rapid onset of spring thaw in the tundra eco-region, with maps of freeze-thaw state showing that this area thawed 4–5 days earlier than the boreal eco-region in 2013 and 2014 (Steiner et al., 2015). While this is less than 1 week, a study relating the date of thaw to the annual radiation budget estimated that a 4-day shift in freeze/thaw date alters the annual radiation budget by 250 MJ m^{-2}, significantly altering the early season budget (Stone et al., 2002). However, in 2012, the boreal eco-region actually thawed 9 days earlier than the tundra. Considering that fluxes calculated from all years are included in this regression, it is not clear that the difference in seasonal pattern could be explained by differences in thaw date alone. Instead, the difference in the seasonal cycle is more likely a result of the distribution of wetlands. Using a map of wetland extent, it is estimated that 30% of the tundra eco-region can be classified as a seasonal wetland, while only 15% of the boreal eco-region is similarly classified (Bergamaschi et al., 2007). As wetlands are defined by a near-surface water table, methanogenesis can begin when the depth of thaw is much shallower, resulting in a CH$_4$ emissions that can begin much earlier. In Sect. 4.5, the effect of the water table on the relationship between temperature and CH$_4$ flux will be discussed further.

4.4.2 Mountain & ocean eco-regions

To test our assumption that emissions from oceans and mountains did not significantly influence measured [CH$_4$], we calculated fluxes assuming any surface (ocean or terrestrial) could emit CH$_4$. The same eco-region regression was used but included the fraction of the footprint which covered the tundra, boreal, mountain, and ocean regions.

Oceans were a weak CH$_4$ source, emitting an average 2 ± 1 mg m^{-2} d^{-1} across the study months. However, Student t-testing found that the fraction of oceans sampled had a consistently large p-value across the season ($p>0.05$), suggesting that footprint sensitivity in oceans was not correlated with ΔCH$_4$. This is consistent with a recent study of summertime sea-air flux of CH$_4$ around Svalbard, Norway, which measured low boundary layer CH$_4$ enhancements despite substantial surface ocean concentrations of CH$_4$ from subsea clathrate deposits in the high arctic (Myhre et al., 2016).

This regression also indicated that mountains might act as a weak seasonal sink of CH$_4$, with a mean strength of -1 ± 2 mg m^{-2} d^{-1}, consistent with recent regional observations of CH$_4$ in the mineral soils of Greenland (Jørgensen et al., 2015).

However, the statistics ($p > 0.1$) were too weak to confirm this as a regional scale phenomenon in our study region. In light of these results, the oceans and mountains were masked from CH_4 flux estimates, as their inclusion would have diluted the contributions of other land types.

4.5 Temperature dependence of CH_4 flux

The results of the regression analysis described in Sect. 3.6 are listed in Table 1 and indicate the r^2 of the best model, the driving variables, and the functional type for each subset (see Eq. 7). Overall, CH_4 flux was seen to most strongly correlate to variance in a Boltzmann-Arrhenius function of T_{40} and the inverse of elevation. While these relationships have been observed in our study region in the past, primarily at the smaller scales of chambers and eddy-covariance towers (e.g. Olefeldt et al., 2013; Sturtevant et al., 2012; Zona et al., 2016), far fewer studies have reported them at a regional scale (Miller et al., 2016; Karion et al., 2016). These latter analyses also identified the inverse elevation (Karion et al., 2016) and sub-surface temperatures (Miller et al., 2016) to be important in explaining the variance of observed CH_4. As in the work of Karion et al. (2016), we used a relatively simple analysis method to arrive at similar explanatory variables as the more sophisticated geostatistical inversion model used by Miller et al. (2016) but with only a subset of the data. Although the r^2 from our analysis may seem low, they are comparable to values derived from regression analysis conducted for chamber studies (Olefeldt et al., 2013). Our results suggest that soil conditions that affect CH_4 flux at the more local scale are also relevant at regional scales.

Since both CH_4 production and flux can be much stronger in wetlands, (e.g. Olefeldt et al., 2013; Sturtevant et al., 2012), the profiles were subdivided into two groups based on the sensitivity of the profiles to wetlands in the domain. When a profile's footprint sensitivity was $\geq 20\%$ wetland by area, the profile was categorized as 'Wetland Present'. Conversely, profiles which had sensitivities $\leq 10\%$ to wetlands by area were categorized as 'Wetland Absent'. The percent of wetland per area sampled by a profile was calculated by averaging a map of wetland fraction (Bergamaschi et al., 2007) weighted by the footprint sensitivity. It was found that for profiles in the Wetlands Absent category, T_{40} and S_{40} were the key predictors in understanding the variability in CH_4 flux, suggesting that CH_4 was being formed lower in the soil column. By contrast, for profiles in the Wetlands Present category, increases in CH_4 flux were correlated with increases in T_{10} and S_{10}.

These two regressions highlight the importance of understanding the depth at which methanogenesis (and methanotrophy) occurs. For instance, in non-wetlands, the water table is deeper than in wetlands. As a result, the onset of CH_4 production in non-wetland regions can significantly lag wetland areas, as the lower section of the soil column will take much longer to thaw. In fact, maps of soil temperature estimate that, on average, soil at 10-cm in the Wetland Present region thawed nearly 3 weeks before soil at 40-cm in the Wetland Absent regions. In addition, soils at these depths and in these regions warmed very differently: T_{10} in the Wetland Present regions increased at an average rate of 0.10 K day^{-1} from point of thaw to the point of annual maximum, while T_{40} in the Wetland Absent regions increased at only 0.06 K day^{-1}. While CH_4 production may occur at any depth within an inundated soil column, CH_4 produced at lower soil depths can be transport limited (depending on bubble formation or aerenchyma); it is, therefore, intuitive that CH_4 produced in wetlands will be more directly correlated to differences in temperature near the surface. Similarly, the dependence of CH_4 production (and ultimately, CH_4 flux) on soil

Atmospheric
Chemistry
and Physics
Discussions

moisture will be most pronounced just beneath the water table, where soil moisture is more susceptible to variability than at lower depths.

These dynamics can be extended to explain the seasonal cycles presented in both Figs. 4 & 6. First, as remarked in Sect. 4.4.1, the tundra eco-region possesses more wetlands than the boreal. As a result, the delayed thaw of the 40-cm soil in combination with slower warming likely explains the delay in boreal eco-region CH_4 flux. Second, while maps of footprint sensitivity across all years showed relatively consistent sensitivity to the tundra in the west and southwest of Alaska (see Figs. 1 & 2), they showed that our measurements were most sensitive to the North Slope of Alaska in 2012, relative to the boreal eco-region. On average, ∼30%, 20%, and 20% of the footprint sensitivity was from regions classified as tundra in 2012 – 2014, respectively. Since the tundra region possesses more seasonal wetlands, it is therefore not surprising that the 2012 seasonal cycle of CH_4 flux in Fig. 4 is closer to the tundra eco-region in Fig. 6, while the 2013 and 2014 seasonal cycles more closely resemble that of the boreal eco-region. However, as the tundra only represents 18% of the total area of interest it is likely that the sampling in 2013 and 2014 was representative of the eco-regions with respect to their total area, while the sampling in 2012 may have been over-sensitive to the tundra.

Overall, sub-surface soil temperature was seen to be the single best explanatory variable throughout the regression analysis. Following the work of Zona et al. (2016), the seasonal cycles of CH_4 flux are plotted versus soil temperature and coloured by days since thaw in Fig. 7. In this figure, CH_4 flux estimates from individual profiles are shown in black points. To highlight the average seasonal trend, these individual estimates were block-averaged into 5-day bins of days since thaw based on satellite retrievals of thaw state (coloured points), before being smoothed by a lowess-filter which locally averaged 35%, or 80-days, of the seasonal cycle (coloured line) (Steiner et al., 2015). Flux estimates from May 2014 were suspected of being over-estimated and were thus excluded from this plot and the regression that follows.

Of the three depths presented in Fig. 7, the seasonal cycle of CH_4 flux has the most consistent, monotonic relationship with T_{40} throughout the study, while the other depths, especially the individual profiles (small black points) show more scatter. We conjecture that the monotonicity of the relationship between T_{40} and CH_4 we observe for our study region is reflective of the fact that CH_4 production is, on average, taking place near this soil level. Evidence for the production of CH_4 at soil depths well below the surface have been reported at the eddy-covariance scale before. In particular, the counterclockwise hysteresis loop in our observations of T_{10} and CH_4 flux is very similar to the relationship observed by eddy-covariance towers at Ivotuk between CH_4 and T_{15} (Zona et al., 2016). Wheras observations of CH_4 flux in wetland sites exhibited a clockwise "hysteresis" loop, the Ivotuk site itself was much drier than other eddy-covariance sites compared in the study, leading the authors to conclude that the direction of the loop was related to whether CH_4 production was occuring above (clockwise) or below (counterclockwise) the soil depth at which temperature was measured (Zona et al., 2016). Similarly, an eddy-covariance tower near Fairbanks, AK, also observed a counterclockwise hysteresis loop when CH_4 flux was plotted against T_{20} (Iwata et al., 2015). It is therefore reasonable to believe that CH_4 production is occuring at depths of ∼40-cm in the broader Wetland Absent regions as a result of a lower water table. In particular, these drier regions play a large role in the late season (September – December) budget, as the production of CH_4 at soil depths well beneath the surface enables CH_4 flux to continue even after the surface soil has begun to freeze (Zona et al., 2016). In the specific case of Ivotuk, CH_4 emitted after the surface had frozen represented nearly 30%

of the total annual budget (Zona et al., 2016). Since "Wetland Absent" regions make up 50% of the surface area of the tundra and boreal eco-regions it is important that these regions are not overlooked when modelling CH_4 emissions at a regional scale.

From Fig. 7, we fit the mean CH_4 flux and T_{40} from the 5-day means to a Boltzmann-Arrhenius equation and determined an activation energy of 0.75 ± 0.20 eV. This value is slightly lower than but still within uncertainties of the global mean activation

5   energy of 0.96 eV (0.86 – 1.07 eV, 95% C.I.) calculated using CH_4 flux measurements from static chambers (Yvon-Durocher et al., 2014). Using T_{40} from NARR in this parameterization, we estimate May–September emissions from our study region to be 2.1 ± 0.3 Tg, 1.8 ± 0.3 Tg and 2.0 ± 0.3 Tg for 2012–2014, respectively (only integrating over non-mountainous areas). This simple model does a remarkable job of capturing the growing season budget estimated from the aircraft observations as well as the timing of the peak in CH_4 emissions. As more winter time measurements would be necessary to properly constrain

10   cold season fluxes, estimates of total annual budgets based on this model are not reported.

5   Conclusions

Analysis of CH_4 column enhancements supplemented by simulated atmospheric transport allowed us to estimate the monthly mean CH_4 fluxes from our study domain (50–75 N, 130–170 W). We estimate that domain averaged CH_4 flux ranged from 2.0–36 mg m^{-2} d^{-1} and that 2.1 ± 0.5 Tg, 1.7 ± 0.4 Tg, and 2.0 ± 0.3 Tg CH_4 were emitted from our domain for 2012–2014,

15   respectively. These estimates were consistent with more complex statistical methods, indicating that this relatively simple analytical technique, with only a subset of the data, is sufficient for determining regional scale CH_4 emissions. The methodology and analysis that followed are therefore useful guidelines for regional monitoring programs which suggest that short, regular profiling of different eco-regions supplemented by fine-scale meteorological modelling can be sufficient to characterize the regional dynamics of the carbon cycle.

20   Despite the lack of spatial resolution within the CH_4 flux estimates, we were able to leverage the atmospheric transport model to inform some basic regression models on how CH_4 flux co-varied with different soil variables and characteristics. We found that when we sampled wetlands, CH_4 flux co-varied most significantly with T_{10}. Conversely, when wetlands were absent, CH_4 flux co-varied with T_{40}. These two results are consistent with observations of how the water table affects the anaerobic production of CH_4 at small spatial scales and emphasize that it is a relevant control at regional scales. Across our

25   study region, we were able to reasonably predict the May–September CH_4 budget using a Boltzmann-Arrhenius model relating CH_4 flux to T_{40}.

Overall, these regressions provide insight in the differences in seasonal cycles observed across the years and eco-regions. Methanogenesis in wetlands (like the tundra) occur closer to the surface since the water table depth is higher. By contrast, methanogenesis occurs lower in the soil column in regions with less wetlands (i.e. boreal regions). Since surface soils will

30   thaw earlier in the season than deeper soils, CH_4 production begins earlier in wetland regions and ends later in drier regions. As a result, campaigns like CARVE, who sample across eco-regions need to be cautious to evenly sample regions with different subsurface hydrology. Overall our results show that factors found to affect CH_4 emissions at scales of 1 m to 1 km are still relevant at the regional scale, suggesting that regional emissions can scale up local scale studies.

Finally, while meteorological differences affected the springtime freeze-thaw transition and fluxes, there was a distinct lack of interannual variability in the overall May–September budget. While observations of CH_4 of flux in northern Alasks have proven to be stable at the scale of eddy covariance towers, this study provides additional regional scale evidence that biogenic CH_4 fluxes in the domain of study are stable at the multi-year time scale.

Atmospheric
Chemistry
and Physics

Discussions

References

Bean, B. R. and Dutton, E.: Radio meteorology, Dover Publications, 1966.

Bergamaschi, P., Frankenberg, C., Meirink, J., Krol, M., Dentener, F., Wagner, T., Platt, U., Kaplan, J., Körner, S., Heimann, M., et al.: Satellite chartography of atmospheric methane from SCIAMACHY on board ENVISAT: 2. Evaluation based on inverse model simulations, Journal of Geophysical Research: Atmospheres, 112, 2007.

Bergamaschi, P., Houweling, S., Segers, A., Krol, M., Frankenberg, C., Scheepmaker, R. A., Dlugokencky, E., Wofsy, S. C., Kort, E. A., Sweeney, C., Schuck, T., Brenninkmeijer, C., Chen, H., Beck, V., and Gerbig, C.: Atmospheric CH4 in the first decade of the 21st century: Inverse modeling analysis using SCIAMACHY satellite retrievals and NOAA surface measurements, J. Geophys. Res., 118, 7350–7369, doi:10.1002/jgrd.50480, http://dx.doi.org/10.1002/jgrd.50480, 2013.

Blake, L., Ovreas, L., Head, I., and Gray, N.: Response of Methanogens in Arctic Sediments to Temperature and Methanogenic Substrate Availability, PLoS ONE, 10, 2015.

Bromwich, D. H., Hines, K. M., and Bai, L.: Development and testing of Polar Weather Research and Forecasting model: 2. Arctic Ocean, J. Geophys. Res., 114, D08 122, doi:10.1029/2008JD010300, 2009.

Bruhwiler, L., Dlugokencky, E., Masarie, K., Ishizawa, M., Andrews, A., Miller, J., Sweeney, C., Tans, P., and Worthy, D.: CarbonTracker-CH4: an assimilation system for estimating emissions of atmospheric methane, Atmospheric Chemistry and Physics, 14, 8269–8293, doi:10.5194/acp-14-8269-2014, http://www.atmos-chem-phys.net/14/8269/2014/, 2014.

Burnham, K. P., Anderson, D. R., and Huyvaert, K. P.: AIC model selection and multimodel inference in behavioral ecology: some background, observations, and comparisons, Behavioral Ecology and Sociobiology, 65, 23–35, 2011.

Chan, K. M. and Wood, R.: The seasonal cycle of planetary boundary layer depth determined using COSMIC radio occultation data, Journal of Geophysical Research: Atmospheres, 118, 2013.

Chang, R. Y.-W., Miller, C. E., Dinardo, S. J., Karion, A., Sweeney, C., Daube, B. C., Henderson, J. M., Mountain, M. E., Eluszkiewicz, J., Miller, J. B., et al.: Methane emissions from Alaska in 2012 from CARVE airborne observations, Proceedings of the National Academy of Sciences, 111, 16 694–16 699, 2014.

Chen, H., Winderlich, J., Gerbig, C., Hoefer, A., Rella, C. W., Crosson, E. R., Pelt, A. D. V., Steinbach, J., Kolle, O., Beck, V., Daube, B. C., Gottlieb, E. W., Chow, V. Y., Santoni, G. W., and Wofsy, S. C.: High-accuracy continuous airborne measurements of greenhouse gases (CO_2 and CH_4) using the cavity ring-down spectroscopy (CRDS) technique, Atmos. Meas. Tech., 3, 375–386, 2010.

Chen, Y.-H. and Prinn, R. G.: Estimation of atmospheric methane emissions between 1996 and 2001 using a three-dimensional global chemical transport model, J. Geophys. Res., 111, D10 307, doi:10.1029/2005JD006058, 2006.

Chou, W. W., Wofsy, S. C., Harriss, R. C., Lin, J. C., Gerbig, C., and Sachse, G. W.: Net fluxes of CO 2 in Amazonia derived from aircraft observations, J. Geophys. Rese., 107, 4614, doi:10.1029/2001JD001295, http://www.agu.org/pubs/crossref/2002/2001JD001295.shtml, 2002.

Christensen, T.: Methane emission from Arctic tundra, Biogeochemistry, 21, 117–139, doi:10.1007/BF00000874, http://dx.doi.org/10.1007/BF00000874, 1993.

Ciais, P., Sabine, C., Bala, G., Bopp, L., Brovkin, V., Canadell, J., Chhabra, A., DeFries, R., Galloway, J., Heimann, M., et al.: Carbon and other biogeochemical cycles, in: Climate change 2013: the physical science basis. Contribution of Working Group I to the Fifth Assessment Report of the Intergovernmental Panel on Climate Change, pp. 465–570, Cambridge University Press, 2014.

Atmospheric
Chemistry
and Physics
Discussions

Collins, M., Knutti, R., Arblaster, J., Dufresne, J.-L., Fichefet, T., Friedlingstein, P., Gao, X., Gutowski, W., Johns, T., Krinner, G., Shongwe, M., Tebaldi, C., Weaver, A., and Wehner, M.: Long-term Climate Change: Projections, Commitments and Irreversibility, book section 12, p. 1029–1136, Cambridge University Press, Cambridge, United Kingdom and New York, NY, USA, doi:10.1017/CBO9781107415324.024, www.climatechange2013.org, 2013.

5 Commission for Environmental Cooperation: Ecological regions of North America: toward a common perspective, Tech. rep., Commission for Environmental Cooperation, 1997.

Dlugogencky, E.: Trends in Atmospheric Methane, Tech. rep., National Oceanic and Atmospheric Administration, www.esrl.noaa.gov/gmd/ccgg/trends_ch4/, date accessed: 01/07/2016, 2016.

Dlugokencky, E., Myers, R., Lang, P., Masarie, K., Crotwell, A., Thoning, K., Hall, B., Elkins, J., and Steele, L.: Conversion of NOAA
10 atmospheric dry air CH4 mole fractions to a gravimetrically prepared standard scale, Journal of Geophysical Research: Atmospheres, 110, 2005.

Dlugokencky, E. J., Nisbet, E. G., Fisher, R., and Lowry, D.: Global atmospheric methane: budget, changes and dangers, Philosophical Transactions of the Royal Society of London A: Mathematical, Physical and Engineering Sciences, 369, 2058–2072, 2011.

Earth Systems Research Laboratory (ESRL): NOAA/ESRL calculation of global means, Tech. rep., National Oceanic and Atmospheric
15 Administration, http://www.esrl.noaa.gov/gmd/ccgg/about/global_means.html, date accessed: 01/07/2016, 2016.

Fan, S. M., Wofsy, S. C., Bakwin, P. S., Jacob, D. J., Anderson, S. M., Kebabian, P. L., McManus, J. B., and Kolb, C. E.: Micrometerological Measurements of CH_4 and CO_2 Exchange Between the Atmosphere and Subarctic Tundra, J. Geophys. Res., 97, 16 627–16 643, 1992.

Gatti, L. V., Gloor, M., Miller, J. B., Doughty, C. E., Malhi, Y., Domingues, L. G., Basso, L. S., Martinewski, a., Correia, C. S. C., Borges, V. F., Freitas, S., Braz, R., Anderson, L. O., Rocha, H., Grace, J., Phillips, O. L., and Lloyd, J.: Drought sensitivity of Amazonian carbon
20 balance revealed by atmospheric measurements., Nature, 506, 76–80, doi:10.1038/nature12957, 2014.

Global Monitoring Division: Carbon Cycle Greenhouse Gas Reference Network, Tech. rep., National Oceanic and Atmospheric Administration, http://www.esrl.noaa.gov/gmd/dv/site/PFA.html, date accessed: 08/12/2016, 2016.

Henderson, J. M., Eluszkiewicz, J., Mountain, M. E., Nehrkorn, T., Chang, R. Y.-W., Karion, A., Miller, J. B., Sweeney, C., Steiner, N., Wofsy, S. C., and Miller, C. E.: Atmospheric transport simulations in support of the Carbon in Arctic Reservoirs Vulnerability Experiment
25 (CARVE), Atmospheric Chemistry and Physics, 15, 4093–4116, doi:doi:10.5194/acp-15-4093-2015, 2015.

Hines, K., Bromwich, D., Bai, L., Bitz, C., Powers, J., and Manning, K.: Sea ice enhancements to Polar WRF, Monthly Weather Review, 143, 2363–2385, doi:doi: 10.1175/MWR-D-14-00344.1, 2015.

Hines, K. M. and Bromwich, D. H.: Development and Testing of Polar Weather Research and Forecasting (WRF) Model. Part I: Greenland Ice Sheet Meteorology*, Mon. Weather Rev., 136, 1971–1989, doi:10.1175/2007MWR2112.1, 2008.

30 Hines, K. M., Bromwich, D. H., Bai, L.-S., Barlage, M., and Slater, A. G.: Development and Testing of Polar WRF. Part III: Arctic Land, J. Climate, 24, 26–48, doi:10.1175/2010JCLI3460.1, 2011.

Hugelius, G., Tarnocai, C., Broll, G., Canadell, J., Kuhry, P., and Swanson, D.: The Northern Circumpolar Soil Carbon Database: spatially distributed datasets of soil coverage and soil carbon storage in the northern permafrost regions, Earth System Science Data, 5, 3–13, 2013.

Iwata, H., Harazono, Y., Ueyama, M., Sakabe, A., Nagano, H., Kosugi, Y., Takahashi, K., and Kim, Y.: Methane exchange in a poorly-drained
35 black spruce forest over permafrost observed using the eddy covariance technique, Agricultural and Forest Meteorology, 214, 157–168, 2015.

Jenness, J. S.: Calculating landscape surface area from digital elevation models, Wildlife Society Bulletin, 32, 829–839, 2004.

Atmospheric
Chemistry
and Physics
Discussions

Johnston, C. E., Ewing, S. A., Harden, J. W., Varner, R. K., Wickland, K. P., Koch, J. C., Fuller, C. C., Manies, K., and Jorgenson, M. T.: Effect of permafrost thaw on CO_2 and CH_4 exchange in a western Alaska peatland chronosequence, Environmental Research Letters, 9, 085 004, http://stacks.iop.org/1748-9326/9/i=8/a=085004, 2014.

Jørgensen, C. J., Johansen, K. M. L., Westergaard-Nielsen, A., and Elberling, B.: Net regional methane sink in High Arctic soils of northeast Greenland, Nature Geoscience, 8, 20–23, 2015.

Jorgenson, M. T., Shur, Y. L., and Pullman, E. R.: Abrupt increase in permafrost degradation in Arctic Alaska, Geophysical Research Letters, 33, 2006.

Karion, A., Sweeney, C., Wolter, S., Newberger, T., Chen, H., Andrews, a., Kofler, J., Neff, D., and Tans, P.: Long-term greenhouse gas measurements from aircraft, Atmospheric Measurement Techniques, 6, 511–526, doi:10.5194/amt-6-511-2013, 2013.

Karion, A., Sweeney, C., Miller, J. B., Andrews, A. E., Commane, R., Dinardo, S., Henderson, J. M., Lindaas, J., Lin, J. C., Luus, K. A., Newberger, T., Tans, P., Wofsy, S. C., Wolter, S., and Miller, C. E.: Investigating Alaskan methane and carbon dioxide fluxes using measurements from the CARVE tower, Atmospheric Chemistry and Physics, 16, 5383–5398, doi:10.5194/acp-16-5383-2016, http://www.atmos-chem-phys.net/16/5383/2016/, 2016.

Kirschke, S., Bousquet, P., Ciais, P., Saunois, M., Canadell, J. G., Dlugokencky, E. J., Bergamaschi, P., Bergmann, D., Blake, D. R., Bruhwiler, L., et al.: Three decades of global methane sources and sinks, Nature Geoscience, 6, 813–823, 2013.

Lin, J., Gerbig, C., Wofsy, S., Andrews, A., Daube, B., Davis, K., and Grainger, C.: A near-field tool for simulating the upstream influence of atmospheric observations: The Stochastic Time-Inverted Lagrangian Transport (STILT) model, Journal of Geophysical Research: Atmospheres (1984–2012), 108, 2003.

Miller, S., Miller, C., Commane, R., Chang, R.-W., Dinardo, S., Henderson, J., Karion, A., Lindaas, J., Melton, J., Miller, J., Sweeney, C., Wofsy, S., and Michalak, A.: A multi-year estimate of methane fluxes in Alaska from CARVE atmospheric observations, Global Biogeochemical Cycles, in review, 2016.

Myhre, C. L., Ferré, B., Platt, S., Silyakova, A., Hermansen, O., Allen, G., Pisso, I., Schmidbauer, N., Stohl, A., Pitt, J., et al.: Extensive release of methane from Arctic seabed west of Svalbard during summer 2014 does not influence the atmosphere, Geophysical Research Letters, 43, 4624–4631, 2016.

Nehrkorn, T., Eluszkiewicz, J., Wofsy, S. C., Lin, J. C., Gerbig, C., Longo, M., and Freitas, S.: Coupled weather research and forecasting–stochastic time-inverted lagrangian transport (WRF–STILT) model, Meteorology and Atmospheric Physics, 107, 51–64, 2010.

Novelli, P., Collins, J., Myers, R., Sachse, G., and Scheel, H.: Reevaluation of the NOAA/CMDL carbon monoxide reference scale and comparisons with CO reference gases at NASA-Langley and the Fraunhofer Institut, Journal of Geophysical Research: Atmospheres, 99, 12 833–12 839, 1994.

Olefeldt, D., Turetsky, M. R., Crill, P. M., and McGuire, A. D.: Environmental and physical controls on northern terrestrial methane emissions across permafrost zones, Global change biology, 19, 589–603, 2013.

Osterkamp, T.: The recent warming of permafrost in Alaska, Global and Planetary Change, 49, 187–202, 2005.

Overland, J., Hanna, E., Hanssen-Bauer, I., Kim, S.-J., Walsh, J., Wang, M., Bhatt, U., and Thoman, R.: Arctic Report Card 2015: Surface Air Temperatures, Tech. rep., National Oceanic and Atmospheric Administration, http://www.arctic.noaa.gov/reportcard, 2015.

Sasakawa, M., Shimoyama, K., Machida, T., Tsuda, N., Suto, H., Arshinov, M., Davydov, D., Fofonov, A., Krasnov, O., Saeki, T., Koyama, Y., and Maksyutov, S.: Continuous measurements of methane from a tower network over Siberia, Tellus B, 62, 403–416, doi:10.1111/j.1600-0889.2010.00494.x, http://www.tellusb.net/index.php/tellusb/article/view/16583, 2010.

Schuur, E., McGuire, A., Schädel, C., Grosse, G., Harden, J., Hayes, D., Hugelius, G., Koven, C., Kuhry, P., Lawrence, D., et al.: Climate change and the permafrost carbon feedback, Nature, 520, 171–179, 2015.

Skamarock, W., Klemp, J., Dudhia, J., Gill, D., Barker, D., Wang, X.-Y., Wang, W., and Powers, J.: A Description of the Advanced Research WRF Version 3, Tech. rep., MMM Division, NCAR, http://www.mmm.ucar.edu/wrf/users/docs/arw_v3.pdf, 475+STR, 2008.

5 Steiner, N., McDonald, K., Dinardo, S., and Miller, C.: Snowmelt and Surface Freeze/Thaw Timings over Alaska derived from Passive Microwave Observations using a Wavelet Classifier, American Geophysical Union, San Francisco, CA, 14-18 December 2015, 2015.

Stone, R. S., Dutton, E. G., Harris, J. M., and Longenecker, D.: Earlier spring snowmelt in northern Alaska as an indicator of climate change, Journal of Geophysical Research: Atmospheres (1984–2012), 107, ACL–10, 2002.

Stull, R. B.: An introduction to boundary layer meteorology, vol. 13, Springer Science & Business Media, 1988.

10 Sturtevant, C., Oechel, W., Zona, D., Kim, Y., and Emerson, C.: Soil moisture control over autumn season methane flux, Arctic Coastal Plain of Alaska, Biogeosciences, 9, 1423–1440, 2012.

Sweeney, C., Dlugokencky, E., Miller, C., Wofsy, S., Karion, A., Dinardo, S., Chang, R. Y.-W., Miller, J., Bruhwiler, L., Crotwell, A., et al.: No significant increase in long-term CH4 emissions on North Slope of Alaska despite significant increase in air temperature, Geophysical Research Letters, 2016.

15 Tarnocai, C., Canadell, J., Schuur, E., Kuhry, P., Mazhitova, G., and Zimov, S.: Soil organic carbon pools in the northern circumpolar permafrost region, Global biogeochemical cycles, 23, 2009.

Whalen, S.: Biogeochemistry of methane exchange between natural wetlands and the atmosphere, Environmental Engineering Science, 22, 73–94, 2005.

Xue, K., M. Yuan, M., J. Shi, Z., Qin, Y., Deng, Y., Cheng, L., Wu, L., He, Z., Van Nostrand, J. D., Bracho, R., Natali, S., Schuur, E.
20 A. G., Luo, C., Konstantinidis, K. T., Wang, Q., Cole, J. R., Tiedje, J. M., Luo, Y., and Zhou, J.: Tundra soil carbon is vulnerable to rapid microbial decomposition under climate warming, Nature Climate Change, http://dx.doi.org/10.1038/nclimate2940, 2016.

Yvon-Durocher, G., Allen, A. P., Bastviken, D., Conrad, R., Gudasz, C., St-Pierre, A., Thanh-Duc, N., and Del Giorgio, P. A.: Methane fluxes show consistent temperature dependence across microbial to ecosystem scales, Nature, 507, 488–491, 2014.

Zhang, J. and Rothrock, D.: Modeling global sea ice with a thickness and enthalpy distribution model in generalized curvilinear coordinates,
25 Monthly Weather Review, 131, 845–861, 2003.

Zhao, C. L. and Tans, P. P.: Estimating uncertainty of the WMO mole fraction scale for carbon dioxide in air, Journal of Geophysical Research: Atmospheres, 111, 2006.

Zona, D., Gioli, B., Commane, R., Lindaas, J., Wofsy, S. C., Miller, C. E., Dinardo, S. J., Dengel, S., Sweeney, C., Karion, A., et al.: Cold season emissions dominate the Arctic tundra methane budget, Proceedings of the National Academy of Sciences, 113, 40–45, 2016.

Atmospheric
Chemistry
and Physics
Discussions

Table 1. Correlation coefficients and predictors of CH_4 emissions for various linear regression models

N	Subset Condition	r^2	Predictors	Type
		All		
68	–	0.36	T_{40}, Z	Boltz.-Arrh., Inv.
		Sub-sets		
27	Wetlands Present	0.40	T_{10}, S_{10}	Boltz.-Arrh., Lin.
28	Wetlands Absent	0.48	T_{40}, S_{40}	Boltz.-Arrh., Lin.

T_x: mean sampled x-cm subsoil temperature from NARR (K); S_x: mean sampled x-cm subsoil liquid moisture fraction from NARR (-); Z: soil surface elevation above sea-level (km).
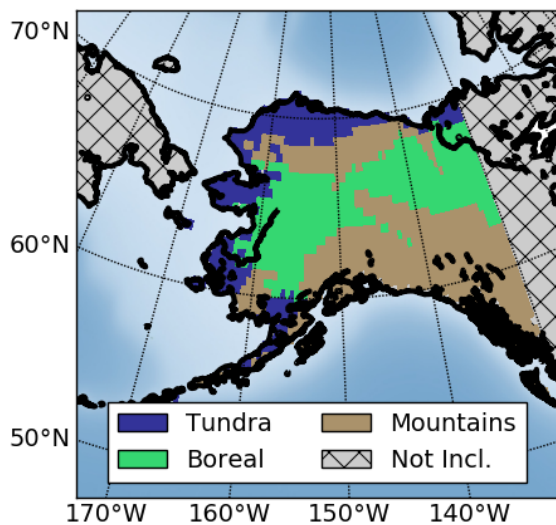
Figure 1. Eco-regions derived from the Commission for Environmental Cooperation Level II Terrestrial Eco-regions. The study region is defined by the coastline and filled eco-regions.

Atmospheric
Chemistry
and Physics
Discussions

Open Access
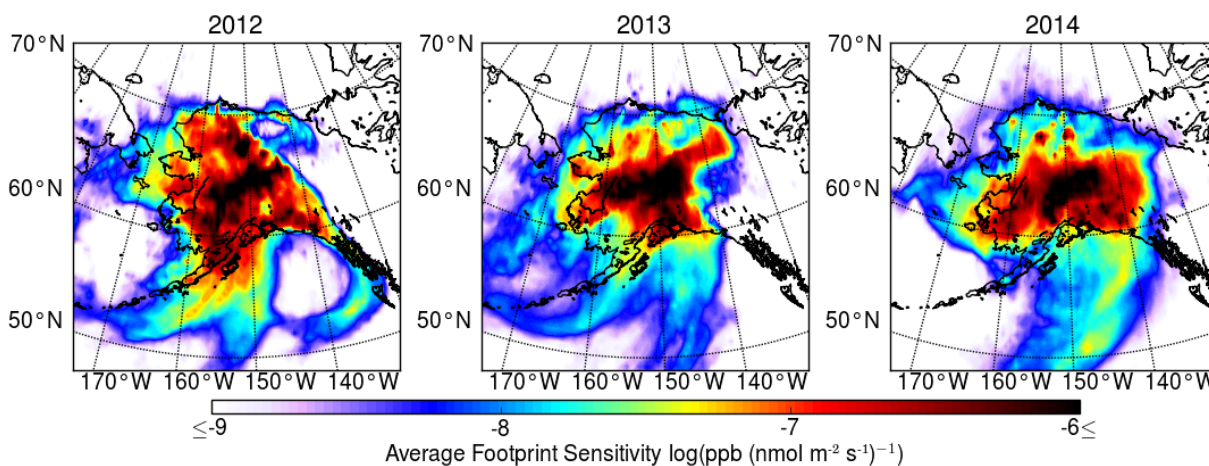
Figure 2. The average footprint sensitivity calculated from WRF-STILT is shown for all receptor points modelled within the profiles included in the analysis (2012–2014).
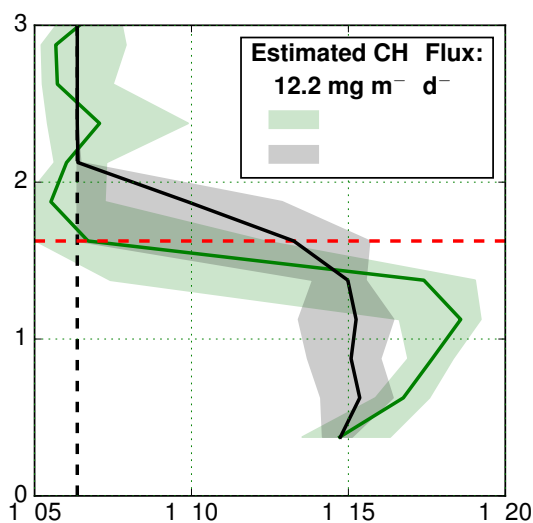

Figure 3. A sample profile from 3 Sep 2014 at 65°N, 148.6°W. Shaded regions denote the minimum/maximum of the ranges and the solid line is the median. The dashed red line represents h, and the dashed black line is $[CH_4]_0$.
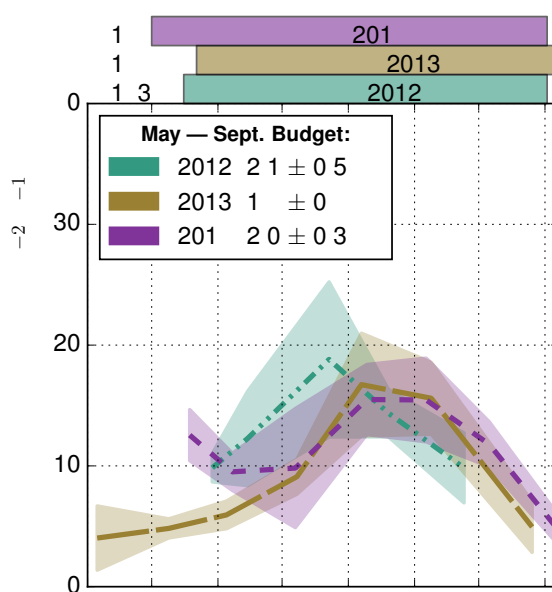
Figure 4. Monthly mean CH_4 flux estimates. Values are centered on the mean measurement date for a given month and the shaded regions are the standard error of the mean. The bar plot above the graph marks the days when average soil temperatures from NARR were above zero, with the total number of unthawed days given by n.
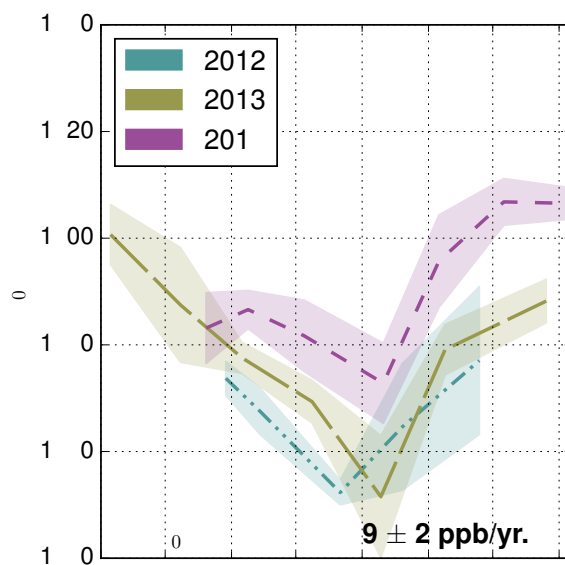
Figure 5. The mean tropospheric $[CH_4]_0$ estimated from profiles (shaded areas indicate 1σ). Values are centered on the mean measurement date.
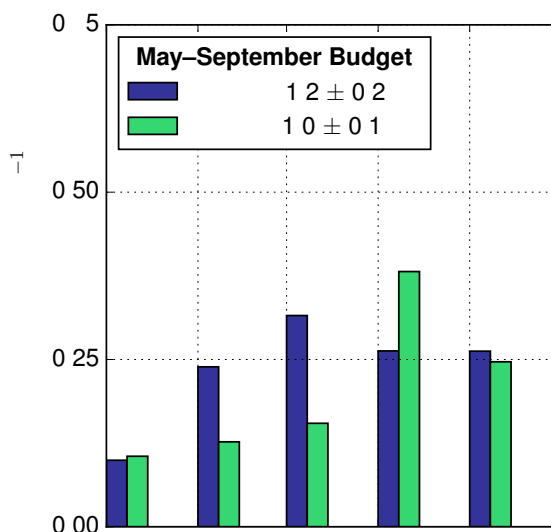
Figure 6. Estimated CH_4 emissions from tundra and boreal eco-regions averaged over all years.
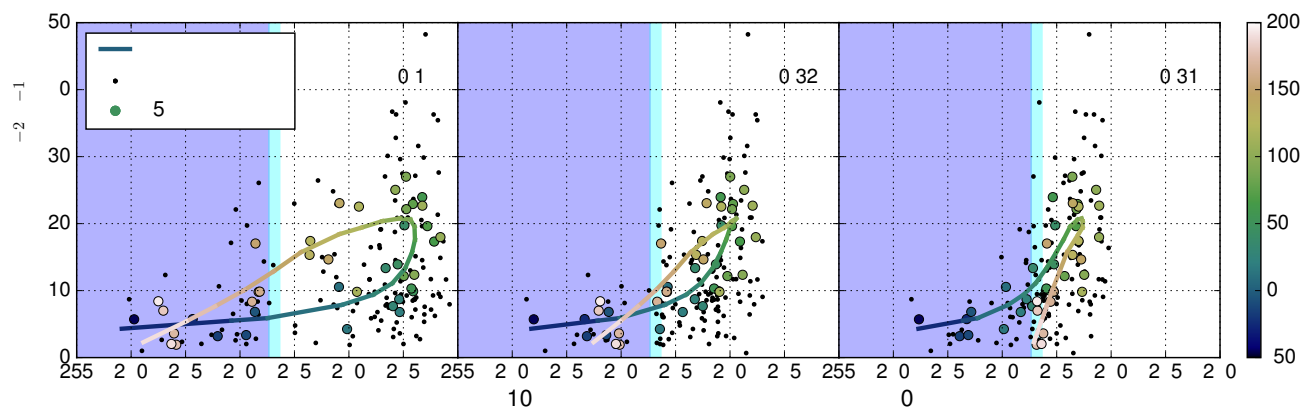
Figure 7. (a – c) CH_4 flux estimates from atmospheric profiles are shown versus footprint-weighted mean soil temperatures at different depths. The shaded background denotes when the soil temperature was at (cyan) or below (blue) the fusion point of water.